Journal of Materials Chemistry A

Accepted Manuscript

ROYAL SOCIETY OF CHEMISTRY

www.rsc.org/materialsA

Tree-like Nanoporous WO_3 Photoanode with Enhanced Charge Transport Efficiency for Photoelectrochemical Water Oxidation

*Sun Shin[a,d,1], Hyun Soo Han[a,b,1], Ju Seong Kim[a], Ik Jae Park[a], Myeong Hwan Lee[a], Kug Sun Hong[a] and In Sun Cho[c,]**

[a]Department of Materials Science and Engineering, Seoul National University, Seoul 151-744, Korea
[b]Department of Mechanical Engineering, Stanford University, Stanford, CA 94306, United States
[c]Department of Materials Science and Engineering & Energy Systems Research, Ajou University, Suwon 443-749, Korea
[d]Engineering Research Institute, Ajou University, Suwon 443-749, Korea

Corresponding Author:
E-mail: insuncho@ajou.ac.kr

[1] These authors contributed equally to this work.

Abstract

We report a tree-like nanoporous tungsten trioxide (WO_3) photoanode that largely improves a photoelectrochemical water oxidation performance. These novel WO_3 photoanodes were prepared using a pulsed laser deposition method and their porosity was controlled by adjusting the oxygen partial pressure during the deposition process. The tree-like nanoporous WO_3 photoanode has a nanoporous structure with a partially preferred alignment of the individual WO_3 nanocrystals, which greatly improves the charge transport efficiency. Under a simulated solar light illumination, the aforementioned features resulted in ~9 times higher photocurrent density (1.8 mA/cm^2 at 1.23 V vs. RHE) than a dense WO_3 photoanode. An incident photon-to-current conversion efficiency of over 70 % was also obtained at wavelengths of 350–400 nm.

Keywords: Hierarchical nanostructure, WO_3, nanoporous, pulsed laser deposition, solar water splitting, charge transport

Introduction

Direct solar-to-hydrogen conversion by photoelectrochemical (PEC) water splitting is an attractive technology for the generation of hydrogen as a renewable and carbon-free fuel. Research on PEC water splitting has spanned four decades since the seminal report by Fujishima and Honda in 1972 that described the successful photoelectrolysis of water using a TiO_2 electrode.[1] Since then, a number of semiconductor materials have been investigated for use in PEC cells. In particular, metal oxide semiconductors such as Fe_2O_3, $BiVO_4$, and WO_3, which have good chemical stability, have been widely studied as photoanodes.[2-4] WO_3 has a moderate band gap (~2.7 eV) and it is preferred over Fe_2O_3 or $BiVO_4$ as a photoanode material because of its good charge carrier transport property (*i.e.*, high electron mobility ~10 cm^2/V-sec and large hole diffusion length ~150 nm).[5-9] So far, there have been a number of studies on the WO_3 photoanodes to improve its PEC water-splitting performance.[10-14] In particular, porous structured WO_3 films prepared by sol-gel and anodization methods showed enhanced photoelectrochemical characteristics such as large surface area and good permeation of electrolyte, which in turn largely increase the PEC performance.[12, 14, 15] Despite some advances, however, the PEC water splitting performance of the WO_3 photoanode is still need to be improved because the generated photocurrent density is lower than the theoretically predicted value (~4.5 mA/cm^2).

Recent developments in nanotechnology for synthesizing nano-materials have triggered significant research interest in PEC water splitting owing to their controllable structure/morphology, and electronic and optical properties.[16-18] Novel three-dimensional (3D) architectures comprising one-dimensional (1D) nanowires/nanorods or two-dimensional (2D) nanoplates received particular attention owing to their unique properties namely, (i) large surface area/active sites, (ii) high light scattering/absorption, (iii) open channels for infiltration of the electrolyte, and (iv) good charge transport within the nanowire or nanoplate trunk.[19-27] In addition, the 3D architectures are beneficial for hetero-junctioning with other photoanode materials to improve the PEC performance further.[28, 29] Several methods based on two-step processes such as hydro/solvo-thermal, vapor-liquid-vapor (VLS), and electrospinning were developed to synthesize these 3D architectures.[5, 24, 30-33] The 3D architectures can also be satisfactorily fabricated using a pulsed laser deposition (PLD) technique, which uses a high energy excimer laser to ablate the metal oxide target. This technique was used to synthesize 3D architectures of TiO_2, *i.e.*, quasi 1D nanostructures with hierarchically organized nanoparticles and pores[23] for the application of dye-sensitized solar cells.[34-37]

In this work, PLD was used to synthesize a tree-like nanoporous WO_3 photoanode by controlling the partial pressure of oxygen. This novel WO_3 photoanode consisted of hierarchically organized and densely interconnected nanocrystals. The tree-like nanoporous WO_3 photoanode was found to exhibit a nanoporous structure with a partially preferred alignment of individual WO_3 nanocrystals. Most importantly, the resulting WO_3 photoanode greatly improves the charge transport efficiency together with charge transfer efficiency resulting in a high photocurrent density which is 9 times higher than that of a dense WO_3 photoanode produced by PEC water oxidation.

Results and Discussion

During PLD, the high energy excimer laser ablates the WO_3 target and creates a plasma plum, which is composed of the ablated species. Hierarchical nanostructures of metal oxides were prepared, using this PLD method, by tuning the kinetic energy of the ablated species, while controlling the experimental parameters such as oxygen partial pressure and working temperature.[35] Based on previous studies of TiO_2,[23, 34-39] WO_3 nanostructures with various densities and porosities are synthesized by controlling the oxygen partial pressure during the PLD deposition process. As shown in the SEM images (Figure S1), the oxygen partial pressure greatly affected the morphology of the WO_3 photoanodes. For example, deposition at a low oxygen partial pressure of 50 mTorr resulted in a dense film. The porosity of the WO_3 photoanode increases greatly, however, when the partial pressure is increased to 100–600 mTorr and a tree-like nanoporous structure forms. The formation of this type of hierarchical nanostructure is due to an increase in the probability of collision between the ablated species and the oxygen molecules. These collisions reduce the kinetic energy of the ablated species and, therefore, eventually induce cluster scattering and self-assembly of the ablated species on the substrate.[40-42] Since the as-prepared WO_3 photoanodes have an amorphous phase (Figure S1e), further thermal annealing was conducted at 550 °C for 2 h in air for crystallization to the monoclinic phase. As shown in Figure S2, all the samples maintain the tree-like nanoporous morphology after annealing, albeit with the occurrence of slight grain growth, and the XRD peaks are indexed to the monoclinic WO_3 (JCPDS #83-0950). It should be noted that although the WO_3 photoanodes prepared at 300 and 600 mTorr are maintain their nanoporous morphology from the SEM images, they exhibited loosely interconnected nanoparticles and often detached/crushed from FTO substrate during PEC measurements, thus showing lower photocurrent density values.

Figure 1a shows a representative SEM image of the synthesized WO_3 photoanode which was deposited at an oxygen partial pressure of 100 mTorr (growth time = 45 min) and subsequently annealed at 550 ^{o}C for 2 h (denoted as W-100). It has a tree-like morphology with a one-dimensional (1-D) nanostructure feature (film thickness = 3.2 μm). In addition, the transmission electron microscopy (TEM) image (Figure 1b) clearly shows that an individual cluster consists of a number of nanosized open pores as well as densely interconnected, hierarchically organized WO_3 nanocrystals, which have an average size of ~60 nm. The average size of the nanocrystals was estimated from Scherrer's equation by using a (200) XRD peak at 24.4°; the results are summarized in Table S1. The calculated size of the nanocrystals is approximately 57 nm, which is consistent with the value determined from TEM.

The crystal structure and relative surface area of the W-100 photoanode (synthesized at 100 mTorr, thickness = 3.2 μm) were investigated by XRD and electrochemical capacitive-current measurements, respectively, and compared with those of its W-50 counterpart (synthesized at 50 mTorr, thickness = 3.2 μm). Figure 2a shows typical XRD patterns of the W-50 and W-100 photoanodes. Both have a monoclinic WO_3 crystal structure and peaks from impurity phases were not detected. Interestingly, the relative intensity of the (020) diffraction peak in the W-100 photoanode is much higher than that of the other peaks. This implies that the WO_3 nanocrystals are partially aligned along the [020] direction, *i.e.*, they exhibit a

partially preferred orientation to [010] direction. On the other hand, the higher relative intensity of the (002), (200), and (202) peaks than those of other planes in the W-50 photoanode, implies that the W-50 film is partially aligned along the [101] direction. Therefore, it can be concluded that the oxygen partial pressure during PLD, using an excimer laser, influences both the morphology (*i.e.*, porosity) and the crystal structure (*i.e.*, alignment) of the WO_3 photoanode.[43, 44] The relative electrochemical surface area of the W-100 photoanode was determined from the capacitive-current measurements using cyclic voltammograms (Figure S4).[45-47] As shown in Figure 2b, the nanoporosity of the W-100 photoanode results in a large increase in the specific surface area (~15 times larger than that of the W-50), indicating a good permeation of the electrolyte into the open channels of the WO_3 photoanode.[22, 47]

The optical properties of ~3.2 μm-thick W-50 and W-100 photoanodes were measured for wavelengths in the range of 300–600 nm. These photoanodes were grown on 500 μm-thick quartz substrates in order to minimize the effect of the substrate on the measurements[48]. Figure 3a-c compares the corresponding transmittance (T), reflectance (R), and absorption + scattering (=100 – T – R) spectra of the photoanodes. The transmittance and reflectance of the W-100 photoanode are about 20 % lower than those of the W-50, owing to a strong light scattering effect by its tree-like nanostructure.[20, 36, 49] Furthermore, although the W-50 and W-100 photoanodes have identical absorption edges, *i.e.*, 460 nm (bandgap ~2.7 eV), the latter absorbs more light than the former. This difference stems from the reduced transmittance and reflectance of the W-100, and indicates that this photoanode has a structural advantage for light absorption.

The photoelectrochemical (PEC) water oxidation performance of the WO_3 photoanodes was evaluated using a standard three-electrode system under a simulated solar-light illumination (AM 1.5G, 100 mW/cm^2). Figure 4a shows the corresponding photocurrent density-potential (*J-V*) curves of the W-100 and W-50 photoanodes. The *J-V* curves of the other WO_3 photoanodes, which were prepared at different oxygen partial pressures, are shown in Figure S3. Interestingly, the W-100 photoanode (prepared at 100 mTorr, 3.2 μm thick) exhibits significantly (8 times) higher saturation photocurrent density (J_{sat} = 2.3 mA/cm^2 at ~2.0 V_{RHE}) than that of the W-50 (3.2 μm thick, J_{sat} = 0.3 mA/cm^2 at ~2.0 V_{RHE}). Furthermore, at 1.23 V_{RHE}, which is generally used as a reference potential for comparison, the W-100 photoanode shows 9 times higher photocurrent density (1.8 mA/cm^2) than the W-50 photoanode (0.2 mA/cm^2), demonstrating the tree-like nanoporous WO_3 photoanode has an excellent photoelectrochemical water oxidation performance. The PEC performance of our W-100 photoanode was further compared to previously reported WO_3 photoanodes with various nanostructures (Figure S5). Although the W-100 shows larger onset potential than the others, it shows highest photocurrent density at 1.23 V_{RHE}. The significantly higher photocurrent density of the W-100 photoanode, compared to that of W-50, stems from its structural features, *i.e.*, tree-like morphology and nanoporosity, which enable effective permeation of the electrolyte through the open channels. This effective permeation, in turn, minimizes the hole transport distance to the surface.[3, 12, 15, 22, 47] In addition, the external quantum efficiencies of these photoanodes were quantitatively compared by performing incident photon-to-current conversion efficiency (IPCE) measurements at a potential of 1.23 V_{RHE} (Figure 4b). Compared to the W-50 photoanode, the IPCEs of the W-100 were

considerably higher over the entire range of wavelengths below the band edge (~460 nm). The photocurrent densities at 1.23V_{RHE} were calculated by integrating the IPCE spectra with a standard AM 1.5G solar spectrum (ASTM G-173-03), and were found to be 0.15 and 1.62 mA/cm^2 for the W-50 and W-100 photoanodes, respectively. These values are quite similar to those obtained (0.2 and 1.8 mA/cm^2) from the *J–V* curve. This result indicates that the solar simulator is well-matched to the AM 1.5G light spectrum and the resulting *J-V* measurements are, therefore, reliable. Moreover, IPCEs are, in general, expressed as the product of three factors, namely, the (1) light absorption efficiency (η_{abs}), (2) charge transfer efficiency ($\eta_{transfer}$), and (3) charge transport efficiency ($\eta_{transport}$); *i.e.*,:[50]

$$IPCE = \eta_{abs} \times \eta_{transfer} \times \eta_{transport}$$

As previously shown in Figure 3, the W-100 photoanode absorbs ~20 % more light than the W-50. However, this difference in light absorption does not explain the significantly (9 times) higher photocurrent density value of the former compared to the latter. To understand the large improvement in the PEC performance, a hole scavenger method was used to obtain $\eta_{transfer}$ and $\eta_{transport}$ by adding hydrogen peroxide (H_2O_2) or sodium sulfate (Na_2SO_3) to the electrolyte (Figure S6).[33, 50-52] Figure 5a-b shows the estimated $\eta_{transfer}$ and $\eta_{transport}$ as a function of the applied potential. At a potential of 1.23 V_{RHE}, the W-100 photoanode has a $\eta_{transfer}$ of 78 %, which is slightly higher than that (70 %) of the W-50. The higher $\eta_{transfer}$ of the W-100 photoanode indicates that the nanoporous structure contributes to reducing surface electron–hole recombination by increasing the area of the depletion layer and shortening the hole diffusion distance to the WO_3/electrolyte interface.[22, 52] Owing to the significantly larger surface of the W-100 compared to that of the W-50, correspondingly large differences between the $\eta_{transfer}$ values were expected. The relatively small (~10 %) difference obtained suggests that, compared to the W-50, the W-100 photoanode has lower surface catalytic reactivity due to different exposed facets which limits further increase of the $\eta_{transfer}$.[53]

There are, however, significant differences between the transport efficiency, $\eta_{transport}$, values. With a value of 78 % at 1.23 V_{RHE}, $\eta_{transport}$ of the W-100 photoanode is approximately 9 times higher than that of the W-50 (9%). The enhanced $\eta_{transport}$ of the W-100 results from an increase in the electron and hole transport owing to a reduction in bulk recombination, which is facilitated by its crystal structure and nanoporous features. As shown previously in Figure 2a, the WO_3 nanocrystals in the W-100 have different partial-orientation alignment from those of their W-50 counterparts; *i.e.*, [010] for W-100 vs. [101] for W-50, which might affect the electron mobility and hence, the electron transport properties.[2] Moreover, the nanoporous feature of the W-100 photoanode enables easy permeation of the electrolyte into the photoanode, thereby resulting in a hole diffusion distance that is lower than its hole diffusion length (~150 nm). Figure 5c illustrates the effectiveness of the W-100 photoanode with tree-like nanostructure and nanoporosity for electron and hole transport. Compared to the W-50 photoanode, the nanoporous structure in the W-100 enables intimate contact between the electrolyte and the photoanode surface, even at the bottom. This results in shorter hole diffusion distances to the electrolyte and efficient electron/hole separation. In addition, the partial alignment of the WO_3 nanocrystals aids electron transport to the FTO without a large recombination loss.[54] Therefore, although the light absorption, charge transfer and transport efficiencies simultaneously contribute, the improved PEC water-oxidation performance in W-

100 photoanode is largely attributed to the efficient electron and hole transport/separation due to its unique morphology.

Finally, stability of the W-100 photoanode was tested for 1h by measuring the photocurrent-time (J-t) curves in both phosphate buffer (pH ~7) and sulfuric acid (pH ~0.2) electrolytes. As shown in Figure 6, the W-100 photoanode retains its high photocurrent density after 1 h operation (~18% degradation) in both electrolytes, indicating that the W-100 photoanode is somewhat stable in both acidic and neutral electrolytes at least for 1 h. The faradaic efficiency of the W-100 photoanode for O_2 production was in the range of 55-65% for 1 h (Figure S7).

In summary, a tree-like nanoporous WO_3 photoanode has been prepared by a pulsed laser deposition method through the control of oxygen partial pressure. Compared to a dense WO_3 photoanode, the tree-like nanoporous WO_3 photoanode exhibited a partially preferred orientation to the [010] direction, a large surface area, and an enhanced optical absorption. As it relates to the photoelectrochemical water oxidation reaction, the tree-like nanoporous WO_3 photoanode exhibited much higher photocurrent density, 1.8 mA/cm^2 at 1.23 V_{RHE}, than the dense WO_3 photoanode. This significantly higher photocurrent density results from the greatly improved charge transport property of the nanoporous feature with a partially preferred orientation. In light of the significant improvement in the charge transport efficiency, nanoporous photoanodes, prepared via pulsed laser deposition, which have a partially preferred orientation feature should enable further improvement of the photoelectrochemical water oxidation performance by applying other metal oxides and heterojunction structures.

Experimental Section

Preparation of the WO_3 Photoanode: WO_3 photoanodes with porous nanostructures were prepared on fluorine-doped tin oxide (FTO, Pilkington, TEC8) or quartz substrates by a pulsed laser deposition (PLD) method (KrF excimer laser, 248 nm). The energy density of the laser beam was 1.5 J/cm^2 and the pulse-repetition rate was set at 5 Hz. The WO_3 target (~2 in in diameter) for the PLD was prepared from a pure WO_3 (99.9%, High Purity Chemicals), pressed to a pellet, and sintered at 1000 °C for 10 h in air. The deposition of the WO_3 photoanode was performed by controlling the oxygen partial pressure, which was set to 50, 100, 300, and 600 mTorr at room temperature in order to control the porosity of the WO_3 photoanodes. The distance between the WO_3 target and FTO substrate was fixed to 5 cm. The thickness of the films was adjusted by controlling the deposition time (typically, 30 min). The as-deposited WO_3 photoanodes were crystallized by annealing at 550 ^oC for 2 h in air.

Characterization of samples: The morphology of the WO_3 photoanode was observed by field emission scanning electron microscopy (FE-SEM, SU70, Hitachi) and transmission electron microscopy (TEM, JEM-2100F, JEOL). An X-ray diffractometer (XRD; D-8 Advanced, Bruker) was used to characterize the crystal structure. Optical properties of the samples were measured by using an ultraviolet-visible (UV-VIS) spectrophotometer (Cary 5000, Agilent Technologies) with an integrating sphere. The reflectance (R) and transmittance (T) spectra were obtained by air reference from 300 to 600 nm. The sum of absorption (A) and scattering

(S) was calculated with the formula A + S = 100 – T – R and plotted as a function of the wavelength.

Photoelectrochemical and electrochemical measurements: The PEC performance of the photoanodes were measured using a potentiostat (CHI 608C, CH Instruments) in a three-electrode system with the WO_3 photoanode as a working electrode, a Pt wire as a counter electrode, and 3 M NaCl saturated Ag/AgCl electrode as a reference electrode under simulated solar light illumination (AM 1.5, 100 mW/cm^2, PEC-L11, Percell). The light power was calibrated using a reference cell certified by the National Renewable Energy Laboratories (Model 91150V, Newport, USA). Furthermore, 0.5 M phosphate buffer solution (pH 7) and 0.5 M H_2SO_4 (pH ~0.2) were used as electrolytes after being purged by highly pure argon (99.999 %) to remove the dissolved oxygen. The RHE potential was calculated using the following equation:

$$V_{RHE} = V_{AgCl} + 0.059pH + E_{AgCl}°$$

$$E_{AgCl}°(3\ M\ NaCl) = 0.209\ V\ at\ 25\ °C$$

The relative surface areas of the WO_3 photoanodes were obtained by capacitive current measurements in the potential range of -0.05 - 0.15 V vs. Ag/AgCl (→ 0.57-0.77 V vs. RHE), where all current is only attributed to capacitive charging due to the absence of any redox features in the dark condition by using a phosphate buffer solution under dark condition. We also assumed that the intrinsic specific surface capacitance of all WO_3 films is approximately the same.[55] The scan rates were varied from 25 to 300 mV/s. Moreover, the relative active surface area of the sample was obtained from the slope of the capacitive current vs. scan rate curve. The IPCEs were measured at 1.23 V_{RHE} in a three-electrode system. A 1000 W Xe lamp equipped with a monochromator (CM-110, 1/8, SP Spectra Product) was used to generate a monochromatic beam. The incident light intensity was calibrated by a standard silicon photodiode. In addition, H_2O_2 or Na_2SO_3 was added to the electrolyte solution as a hole scavenger in order to obtain the charge transfer and transport efficiencies. [3, 51]

Acknowledgement

This work was supported by the new faculty research fund of Ajou University (S-2014-G0001-00309).

References

1. A. Fujishima and K. Honda, *Nature*, 1972, **238**, 37-38.
2. A. Kay, I. Cesar and M. Gratzel, *Journal of the American Chemical Society*, 2006, **128**, 15714-15721.
3. T. W. Kim and K. S. Choi, *Science*, 2014, **343**, 990-994.
4. J. Su, X. Feng, J. D. Sloppy, L. Guo and C. A. Grimes, *Nano Lett*, 2011, **11**, 203-208.
5. P. M. Rao, I. S. Cho and X. Zheng, *Proceedings of the Combustion Institute*, 2013, **34**, 2187-2195.
6. M. A. Butler, R. D. Nasby and R. K. Quinn, *Solid State Commun*, 1976, **19**, 1011-1014.
7. M. A. Butler, *Journal of Applied Physics*, 1977, **48**, 1914.
8. J. Zhao, E. Olide and F. E. Osterloh, *Journal of The Electrochemical Society*, 2015, **162**, H65-H71.
9. M. R. Waller, T. K. Townsend, J. Zhao, E. M. Sabio, R. L. Chamousis, N. D. Browning and F. E. Osterloh, *Chemistry of Materials*, 2012, **24**, 698-704.
10. M. Butler, R. Nasby and R. K. Quinn, *Solid State Communications*, 1976, **19**, 1011-1014.
11. H. Wang, T. Lindgren, J. He, A. Hagfeldt and S.-E. Lindquist, *The Journal of Physical Chemistry B*, 2000, **104**, 5686-5696.
12. C. Santato, M. Ulmann and J. Augustynski, *The Journal of Physical Chemistry B*, 2001, **105**, 936-940.
13. B. D. Alexander, P. J. Kulesza, I. Rutkowska, R. Solarska and J. Augustynski, *Journal of Materials Chemistry*, 2008, **18**, 2298-2303.
14. V. Cristino, S. Caramori, R. Argazzi, L. Meda, G. L. Marra and C. A. Bignozzi, *Langmuir*, 2011, **27**, 7276-7284.
15. L. Meda, G. Tozzola, A. Tacca, G. Marra, S. Caramori, V. Cristino and C. A. Bignozzi, *Solar Energy Materials and Solar Cells*, 2010, **94**, 788-796.
16. Z. Wang, S. Zhou and L. Wu, *Advanced Functional Materials*, 2007, **17**, 1790-1794.
17. Y. Baek, Y. Song and K. Yong, *Adv Mater*, 2006, **18**, 3105-3110.
18. J. K. Kim, J. H. Moon, T. W. Lee and J. H. Park, *Chem. Commun.*, 2012, **48**, 11939-11941.
19. J. Shi, Y. Hara, C. Sun, M. A. Anderson and X. Wang, *Nano Lett*, 2011, **11**, 3413-3419.
20. M. J. Bierman and S. Jin, *Energy & Environmental Science*, 2009, **2**, 1050-1059.
21. Z. Yin, Z. Wang, Y. Du, X. Qi, Y. Huang, C. Xue and H. Zhang, *Advanced Materials*, 2012, **24**, 5374-5378.
22. X. Zhao, W. Luo, J. Feng, M. Li, Z. Li, T. Yu and Z. Zou, *Advanced Energy Materials*, 2014, **4**, n/a-n/a.
23. F. Di Fonzo, C. Casari, V. Russo, M. Brunella, A. L. Bassi and C. Bottani, *Nanotechnology*, 2009, **20**, 015604.
24. N. Wang, D. Wang, M. Li, J. Shi and C. Li, *Nanoscale*, 2014, **6**, 2061-2066.
25. X. Liu, F. Wang and Q. Wang, *Physical Chemistry Chemical Physics*, 2012, **14**, 7894-7911.
26. T. Zhu, M. N. Chong and E. S. Chan, *ChemSusChem*, 2014, **7**, 2974-2997.
27. H. M. Chen, C. K. Chen, R.-S. Liu, L. Zhang, J. Zhang and D. P. Wilkinson, *Chemical Society Reviews*, 2012, **41**, 5654-5671.
28. Y. Pihosh, I. Turkevych, K. Mawatari, T. Asai, T. Hisatomi, J. Uemura, M. Tosa, K. Shimamura, J. Kubota, K. Domen and T. Kitamori, *Small*, 2014, **10**, 3692-3699.

29. X. Shi, I. Y. Choi, K. Zhang, J. Kwon, D. Y. Kim, J. K. Lee, S. H. Oh, J. K. Kim and J. H. Park, *Nat Commun*, 2014, **5**.
30. J. Y. Zheng, G. Song, C. W. Kim and Y. S. Kang, *Nanoscale*, 2013, **5**, 5279-5282.
31. S. K. Biswas and J.-O. Baeg, *International Journal of Hydrogen Energy*, 2013, **38**, 3177-3188.
32. Y. Baek, Y. Song and K. Yong, *Advanced Materials*, 2006, **18**, 3105-3110.
33. P. M. Rao, L. Cai, C. Liu, I. S. Cho, C. H. Lee, J. M. Weisse, P. Yang and X. Zheng, *Nano letters*, 2014, **14**, 1099-1105.
34. J. H. Park, D. H. Kim, S. S. Shin, H. S. Han, M. H. Lee, H. S. Jung, J. H. Noh and K. S. Hong, *Advanced Energy Materials*, 2014, **4**, 1300395.
35. J. H. Noh, J. H. Park, H. S. Han, D. H. Kim, B. S. Han, S. Lee, J. Y. Kim, H. S. Jung and K. S. Hong, *The Journal of Physical Chemistry C*, 2012, **116**, 8102-8110.
36. L. Passoni, F. Ghods, P. Docampo, A. Abrusci, J. Marti-Rujas, M. Ghidelli, G. Divitini, C. Ducati, M. Binda and S. Guarnera, *ACS nano*, 2013, **7**, 10023-10031.
37. F. Sauvage, F. Di Fonzo, A. Li Bassi, C. Casari, V. Russo, G. Divitini, C. Ducati, C. Bottani, P. Comte and M. Graetzel, *Nano letters*, 2010, **10**, 2562-2567.
38. Y. Li, X. Fang, N. Koshizaki, T. Sasaki, L. Li, S. Gao, Y. Shimizu, Y. Bando and D. Golberg, *Advanced Functional Materials*, 2009, **19**, 2467-2473.
39. M. Walczak, M. Oujja, J. F. Marco, M. Sanz and M. Castillejo, *Applied Physics A*, 2008, **93**, 735-740.
40. F. Di Fonzo, A. Bailini, V. Russo, A. Baserga, D. Cattaneo, M. Beghi, P. Ossi, C. Casari, A. Li Bassi and C. Bottani, *Catalysis today*, 2006, **116**, 69-73.
41. B. N. Nair, T. Suzuki, Y. Yoshino, S. Gopalakrishnan, T. Sugawara, S. I. Nakao and H. Taguchi, *Advanced Materials*, 2005, **17**, 1136-1140.
42. A. Infortuna, A. S. Harvey and L. J. Gauckler, *Advanced Functional Materials*, 2008, **18**, 127-135.
43. K. Kakimoto, H. Ohsato, H. Kakemoto and Y. Masuda, *Journal of the European Ceramic Society*, 2004, **24**, 993-997.
44. E. Irissou, B. Le Drogoff, M. Chaker and D. Guay, *Journal of applied physics*, 2003, **94**, 4796-4802.
45. A. Pozio, M. De Francesco, A. Cemmi, F. Cardellini and L. Giorgi, *Journal of power sources*, 2002, **105**, 13-19.
46. L. D. Burke and O. J. Murphy, *Journal of Electroanalytical Chemistry and Interfacial Electrochemistry*, 1979, **96**, 19-27.
47. B. A. Pinaud, P. C. K. Vesborg and T. F. Jaramillo, *The Journal of Physical Chemistry C*, 2012, **116**, 15918-15924.
48. I. S. Cho, Z. B. Chen, A. J. Forman, D. R. Kim, P. M. Rao, T. F. Jaramillo and X. L. Zheng, *Nano Letters*, 2011, **11**, 4978-4984.
49. Q. Zhang and G. Cao, *Journal of Materials Chemistry*, 2011, **21**, 6769-6774.
50. I. S. Cho, C. H. Lee, Y. Feng, M. Logar, P. M. Rao, L. Cai, D. R. Kim, R. Sinclair and X. Zheng, *Nat Commun*, 2013, **4**, 1723.
51. H. Dotan, K. Sivula, M. Grätzel, A. Rothschild and S. C. Warren, *Energy & Environmental Science*, 2011, **4**, 958-964.
52. T. W. Kim and K.-S. Choi, *Science*, 2014, **343**, 990-994.
53. Y. P. Xie, G. Liu, L. Yin and H.-M. Cheng, *J Mater Chem*, 2012, **22**, 6746-6751.
54. S. C. Warren, K. Voïtchovsky, H. Dotan, C. M. Leroy, M. Cornuz, F. Stellacci, C. Hébert, A. Rothschild and M. Grätzel, *Nature materials*, 2013, **12**, 842-849.
55. B. A. Pinaud, P. C. Vesborg and T. F. Jaramillo, *The Journal of Physical Chemistry C*, 2012, **116**, 15918-15924.

Figure captions

Figure 1. Morphology of the tree-like nanoporous WO_3 photoanode. (a) A representative SEM image of the WO_3 photoanode grown on the FTO substrate (annealed at 550 ^oC/2h after pulsed laser deposition at an oxygen partial pressure of 100 mTorr, deposition time = 45 min, thickness=3.2 μm), (b) A TEM image of the nanoporous WO_3 cluster. The inset shows a high-resolution TEM image at the rectangular region.

Figure 2. Crystal structure and relative surface area of nanoporous WO_3 photoanode. (a) XRD pattern of the W-100 and W-50 photoanodes (film thickness = 3.2 μm), (b) plot of the linear relationship between capacitive current and scan rate of the W-100 and W-50 photoanodes. As shown in Figure S4, the capacitive current was measured by using cyclic voltammograms with various scan rates in a 0.5 M phosphate buffer solution (pH 7.0).

Figure 3. Optical properties of W-100 and W-50 films grown on quartz substrates (film thickness = 3.2 μm). (a) Transmittance, (b) Reflectance and (c) Light absorption plus scattering (A + S = 100 – R – T).

Figure 4. Photoelectrochemical water oxidation performance of the W-100 and W-50 WO_3 photoanodes (thickness = 3.2 μm). (a) Photocurrent density-potential (J-V) curves measured in a 0.5 M phosphate buffer solution (pH 7.0) under simulated solar light illumination (AM1.5G, 100 mW/cm^2), and (b) incident photon-to-current conversion efficiency (IPCEs) measured at 1.23 V_{RHE} (=0.608 $V_{Ag/AgCl}$) in a 0.5 M phosphate buffer solution (pH 7.0).

Figure 5. Evaluation of (a) charge transfer and (b) separation/transport efficiencies. The dotted line indicates 1.23V_{RHE}. (c) Schematic illustrations of charge transport/transfer processes in W-50 and W-100 photoanodes. The hierarchical nanoporous WO_3 photoanode has enhanced charge transport (or separation) and transfer efficiencies due to the open structure as well as partial orientation alignment.

Figure 6. Photocurrent-time (J-t) curves of the W-100 photoanode measured at 1.23V vs. RHE in 0.5 M phosphate buffer solution (pH 7.0) and 0.5 M H_2SO_4 electrolyte (pH ~0.2) under simulated solar light illumination (AM1.5G, 100 mW/cm^2).

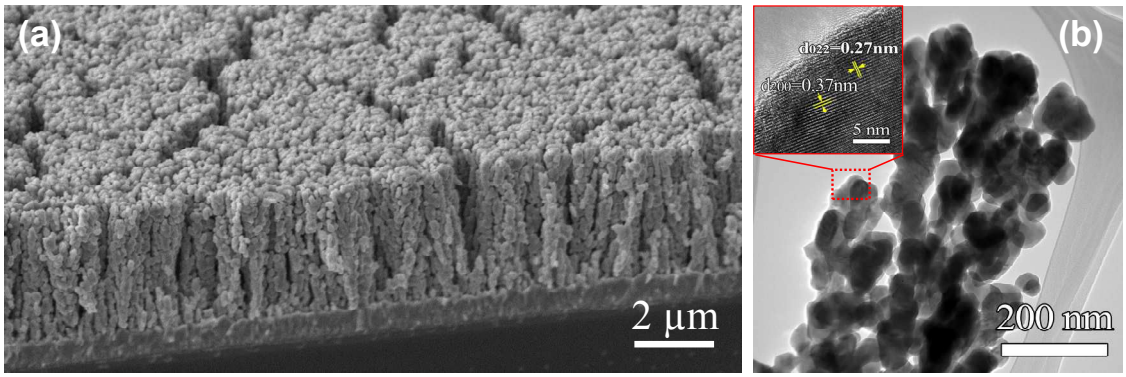

Figure 1. Morphology of the tree-like nanoporous WO_3 photoanode. (a) A representative SEM image of the WO_3 photoanode grown on the FTO substrate (annealed at 550 ^oC/2h after pulsed laser deposition at an oxygen partial pressure of 100 mTorr, deposition time = 45 min, thickness=3.2 μm), (b) A TEM image of the nanoporous WO_3 cluster. The inset shows a high-resolution TEM image at the rectangular region.

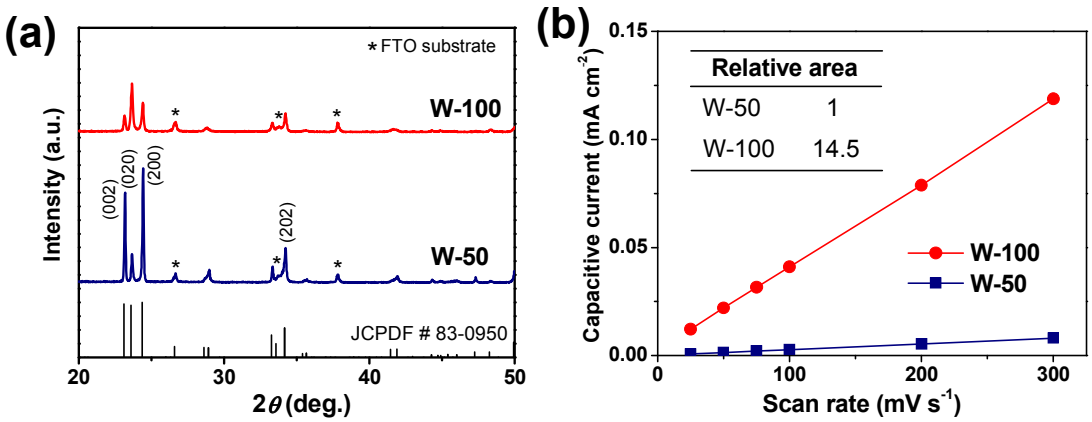

Figure 2. Crystal structure and relative surface area of nanoporous WO_3 photoanode. (a) XRD pattern of the W-50 and W-100 photoanodes (film thickness = 3.2 μm), (b) plot of the linear relationship between capacitive current and scan rate of the W-50 and W-100 photoanodes. As shown in Figure S4, the capacitive current was measured by using cyclic voltammograms with various scan rates in a 0.5 M phosphate buffer solution (pH 7.0).

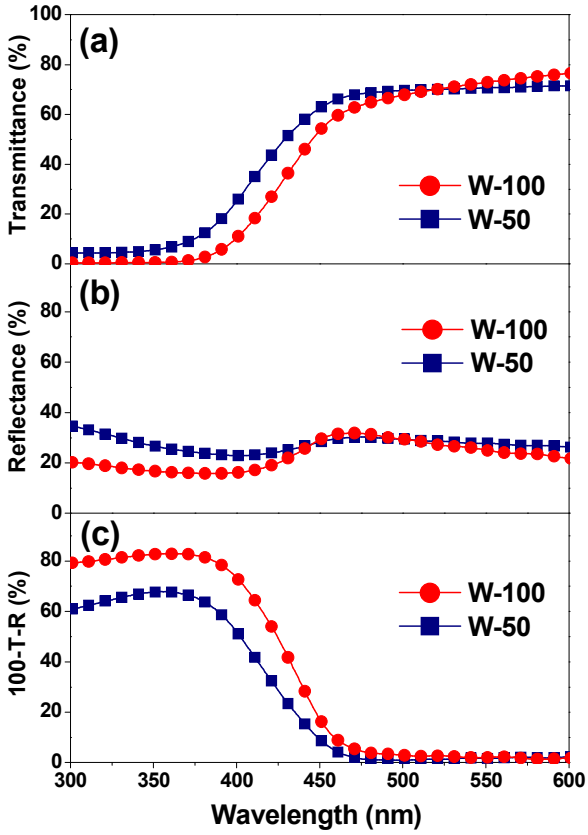

Figure 3. Optical properties of W-100 and W-50 films grown on quartz substrates (film thickness = 3.2 μm). (a) Transmittance, (b) Reflectance and (c) Light absorption plus scattering (A + S = 100 – R – T).

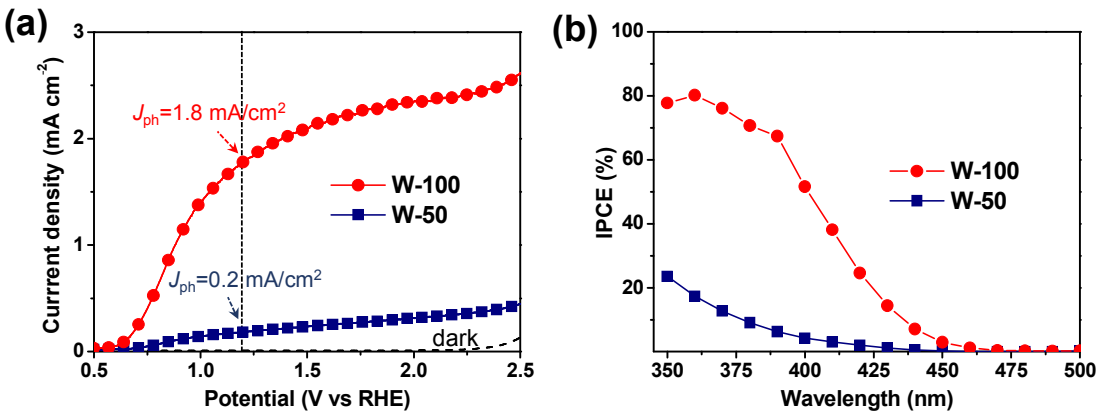

Figure 4. Photoelectrochemical water oxidation performance of the W-100 and W-50 photoanodes (thickness = 3.2μm). (a) Photocurrent density-potential (J-V) curves measured in a 0.5 M phosphate buffer solution (pH 7.0) under simulated solar light illumination (AM1.5G, 100mW/cm^2), and (b) incident photon-to-current conversion efficiency (IPCEs) measured at 1.23V_{RHE} (=0.608 $V_{Ag/AgCl}$) in a 0.5 M phosphate buffer solution (pH 7.0).

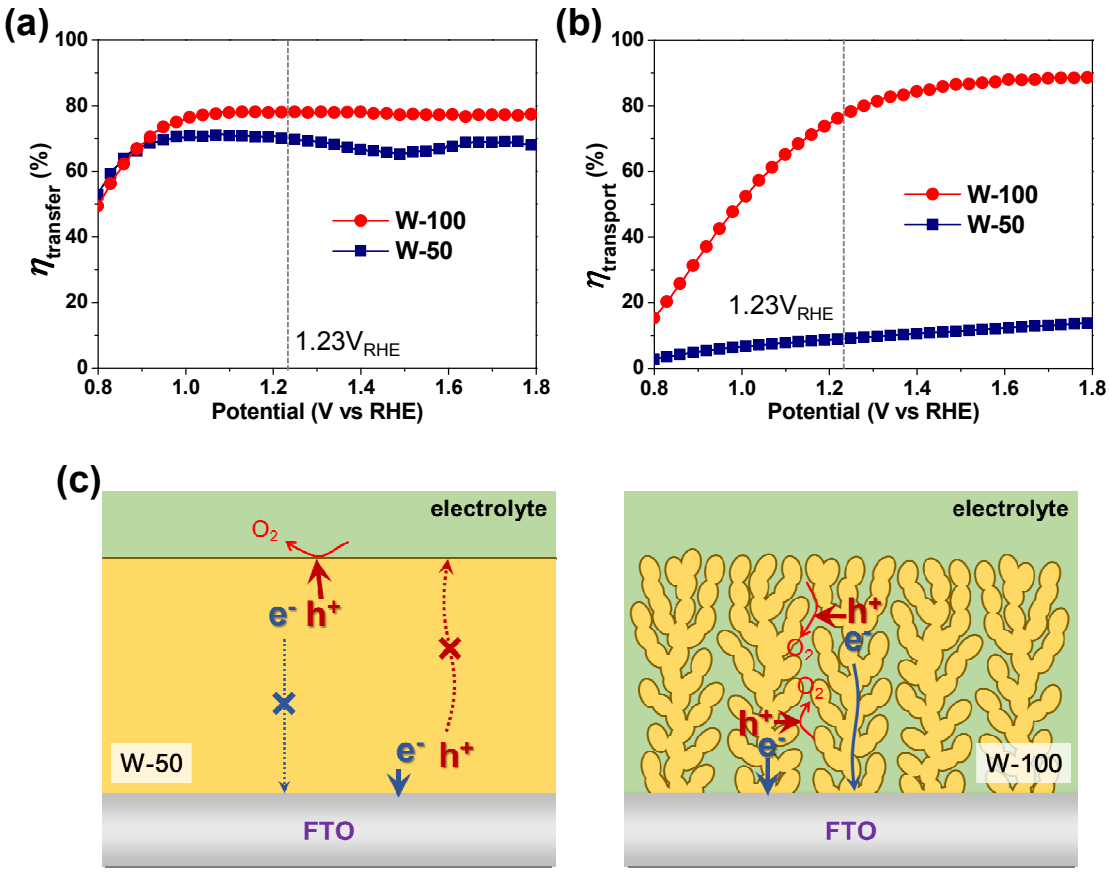

Figure 5. Evaluation of (a) charge transfer and (b) separation/transport efficiencies. The dotted line indicates 1.23V_{RHE}. (c) Schematic illustrations of charge transport/transfer processes in W-50 and W-100 photoanodes. The hierarchical nanoporous WO_3 photoanode has enhanced charge transport (or separation) and transfer efficiencies due to the open structure as well as partial orientation alignment.

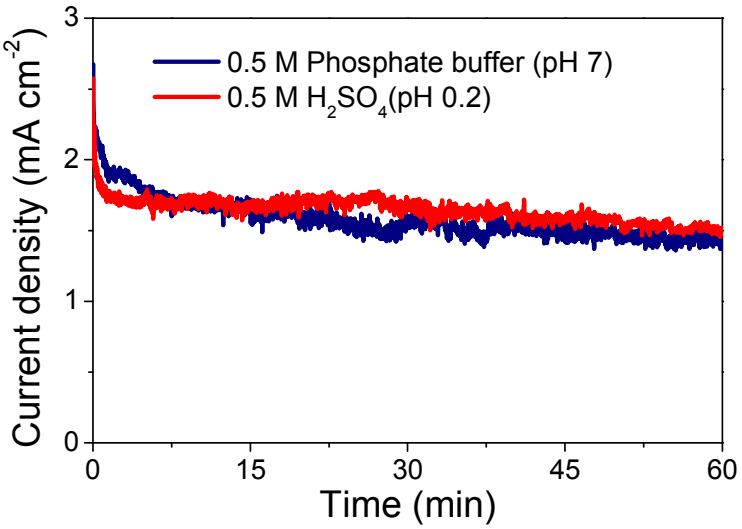

Figure 6. Photocurrent-time (J-t) curves of the W-100 photoanode measured at 1.23V vs. RHE in 0.5 M phosphate buffer solution (pH 7.0) and 0.5 M H_2SO_4 electrolyte (pH ~0.2) under simulated solar light illumination (AM1.5G, 100 mW/cm^2).

Tree-like Nanoporous WO_3 Photoanode with Enhanced Charge Transport Efficiency for Photoelectrochemical Water Oxidation

Sun Shin[a,d,1], *Hyun Soo Han*[a,b,1], *Ju Seong Kim*[a], *Ik Jae Park*[a], *Myeong Hwan Lee*[a], *Kug Sun Hong*[a] *and In Sun Cho*[c,]*

[a]Department of Materials Science and Engineering, Seoul National University, Seoul 151-744, Korea
[b]Department of Mechanical Engineering, Stanford University, Stanford, CA 94306, United States
[c]Department of Materials Science and Engineering & Energy Systems Research, Ajou University, Suwon 443-749, Korea
[d]Engineering Research Institute, Ajou University, Suwon 443-749, Korea

Corresponding Author:
E-mail: insuncho@ajou.ac.kr

[1] These authors contributed equally to this work.

TOC figure

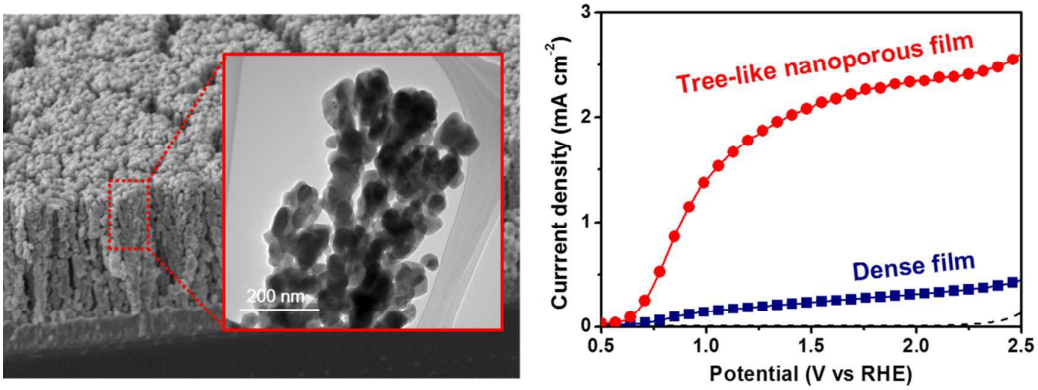

Tree-like nanoporous tungsten trioxide (WO_3) photoanode that largely improves a photoelectrochemical water-oxidation performance was synthesized by a laser ablation method.